

# Grazing-incidence neutron diffraction by thin films with resonance enhancement

Huai Zhang

*Reactor Radiation Division, National Institute of Standards and Technology, Gaithersburg, Maryland 20899  
and Department of Material and Nuclear Engineering, University of Maryland, Maryland 20742*

S. K. Satija, P. D. Gallagher, and J. A. Dura

*Reactor Radiation Division, National Institute of Standards and Technology, Gaithersburg, Maryland 20899*

K. Ritley and C. P. Flynn

*Department of Physics and Materials Research Laboratory, University of Illinois at Urbana-Champaign,  
Urbana, Illinois 61801*

J. F. Ankner

*Missouri University Research Reactor, University of Missouri, Columbia, Missouri 65211*

(Received 15 November 1994; revised manuscript received 21 July 1995)

Diffraction of neutron standing waves in thin films has been demonstrated with experiments on an epitaxially grown Y/Gd/Y/Nb/Al<sub>2</sub>O<sub>3</sub> sample. Resonance enhancement in the diffraction intensity has been observed. The diffraction intensity distribution has been well explained within the distorted-wave Born approximation. The effect of surface miscut and mosaic spread has been incorporated in the quantitative calculation. In general, the proposed diffraction geometry for thin films equally applies for x rays. In contrast to traditional diffraction geometries, the proposed one discriminates against substrate diffraction, provides certain spatial resolution within the film sample, and may be particularly useful when the conventional diffraction geometries for thin films do not apply.

## I. INTRODUCTION

Generally neutron and x-ray diffraction by an imperfect crystal can be adequately described in the kinematic limit, in which the same incident plane wave is scattered by each nucleus or electron without appreciable attenuation or spatial distortion throughout the crystal. In certain cases, however, the to-be-scattered neutron or x-ray wave does not possess the spatial uniformity of a plane wave throughout the crystal. A common example is when absorption or secondary extinction is not negligibly small and thus the original incident plane wave keeps decreasing in amplitude in the direction of travel through the crystal. Another more interesting and deliberate case is the diffraction of evanescent waves near the surface of a bulk crystal.<sup>1-3</sup> An evanescent wave can be created when an incident plane wave is impinged upon the surface at a grazing-incident angle below the critical angle for total external reflection. While traveling parallel to the surface, the evanescent wave has a nonuniform amplitude distribution perpendicular to the surface: its amplitude decreases exponentially into the bulk. One can take advantage of the spatial nonuniformity of the evanescent waves to achieve surface diffraction. In fact, evanescent x-ray and neutron scattering have been widely used to study a broad range of surface phenomena.<sup>1-24</sup>

Recently a diffraction geometry for thin films has been proposed which exploits spatial nonuniformity of a sinusoidal type.<sup>25</sup> In contrast to using the neutron or x-ray

waves *below* a total reflecting surface in evanescent scattering, we propose to use what is *above* a total reflecting surface. Above the reflecting surface, the totally reflected wave interferes with the incident wave near the surface; the superposed wave travels parallel to the surface with a sinusoidally varying amplitude in the direction normal to the surface: it forms a standing wave in the normal direction. If a thin film has been grown on top of the total reflecting surface, the near-surface standing wave may undergo diffraction, which can be used to study the in-plane lattice structures of the thin film. Conventionally, two-dimensional (2D) in-plane lattice structures of a thin film can be studied using neutron or x-ray diffraction either in transmission geometry or, if the lattice is three-dimensional (3D) rather than truly 2D and Bragg peaks from slanted lattice planes are available, in reflection geometry, usually with a four-circle diffractometer in the latter case. Compared to the conventional methods, this diffraction geometry offers three advantages. (1) It discriminates against possible diffraction from the underlying reflecting mirror, which may be a buffer layer or substrate. In particular, the neutron or x-ray wave in the thin film can be resonantly amplified when the spatial period of the standing wave matches the film thickness;<sup>26-29</sup> in such a case the diffraction geometry strongly discriminates against the background from the substrate. (2) As the spatial period of the standing wave can be controlled by varying the incident angle of neutrons or x rays, the diffraction geometry provides certain spatial resolution within the film. (3) If the substrate is highly absorptive,

as is often the case with x rays, diffraction in transmission geometry becomes impossible. Also, it may be inconvenient to use a conventional four-circle diffractometer to study fluid films. In such cases the diffraction geometry can be especially useful. The drawback of the grazing-incidence geometry is that it limits the neutron or x-ray flux intercepted by the thin-film sample, and hence produces weak diffraction intensities. In addition, it requires a substrate or buffer layer which has a higher scattering length density (SLD) than the thin-film sample.

In the remainder of the paper we will report a neutron experiment which implements the ideas described above of using grazing-incidence diffraction geometry for thin films. We choose to use an epitaxially grown Y/Gd/Y/Nb/Al<sub>2</sub>O<sub>3</sub> thin-film sample for several reasons. On one hand, from the technique-development point of view, we would like to start with a sample with known in-plane crystal structures, and the molecular-beam epitaxy (MBE) of single-crystal Gd-Y layers on Nb buffer and Al<sub>2</sub>O<sub>3</sub> substrate is well established.<sup>30,31</sup> In addition, both Nb and Al<sub>2</sub>O<sub>3</sub> have higher neutron SLD than Gd and Y, and thus can conveniently serve as the total reflection mirror. On the other hand, from the physics point of view, we are interested in studying magnetic ordering and magnetic structures of very thin Gd films. The Gd film in the present sample is 3 nm in thickness and is centered symmetrically between the two Y layers. Diffraction by the Gd layer is then expected to be amplified at the first resonance mode and magnetic diffraction to be observed once the Gd orders. Yet, interestingly, no magnetic ordering is seen so far at temperatures as low as 55 K. Further investigation is planned to be carried out at lower temperatures.

The room-temperature results of the present experiment have successfully demonstrated diffraction of neutron standing waves in thin films and the anticipated resonance enhancement in diffraction intensity. The data have been quantitatively well explained using the distorted-wave Born approximation. The effect of surface miscut and mosaic spread has been incorporated in the quantitative calculation.

## II. EXPERIMENTS AND RESULTS

The Y/Gd/Y/Nb/Al<sub>2</sub>O<sub>3</sub> thin-film sample was grown using the MBE technique. Specular x-ray reflectivity measurements were taken to characterize the laterally averaged depth profile of the sample, such as layer thickness and the height of interfacial roughness. X-ray-diffraction measurements were also taken to confirm the in-plane epitaxy of the layers and to determine the surface miscut angles as well as mosaic spread. A careful measurement of the surface miscut angle proves to be critically important in understanding the neutron-diffraction pattern in the grazing-incidence geometry.

### A. Sample preparation

The sample was grown in the Epicenter, a multiple chamber molecular-beam epitaxy facility at the Univer-

sity of Illinois. In one chamber, the substrate, a 3-in wafer of (1 $\bar{1}$ 20)-oriented sapphire (Al<sub>2</sub>O<sub>3</sub>), was degassed and annealed at 1000 °C for approximately 1 h. A nominally 400-nm-thick Nb buffer layer was then deposited at a substrate temperature of 975 °C and growth rate of 0.04 nm s<sup>-1</sup> using an electron beam source. The sample was then cooled to roughly room temperature and transferred within 3 min under a pressure of 5 × 10<sup>-8</sup> torr to a second chamber. In order to remove any surface contamination that formed during transfer, the sample was then heated to 1000 °C for 1 h. Surface quality, as determined by reflection high energy electron diffraction (RHEED), was equal to that of the as-grown Nb film. The Y/Gd/Y layers<sup>30,31</sup> were then grown in this chamber at pressure in the high 10<sup>-10</sup> torr range at a rate of 0.02 nm s<sup>-1</sup>. The first 50-nm Y layer was deposited at 700 °C. Since the epitaxy growth of Gd with minimal interdiffusion into Y requires a lower substrate temperature, the 3-nm Gd layer was grown at 200 °C. The final Y layer was also grown at a low temperature, 175 °C, to minimize interdiffusion. While this temperature was below that typically used for high quality Y growth, the RHEED nevertheless indicated a crystalline surface although with thicker diffraction streaks and weaker Kikuchi lines than the first Y epilayer.

### B. Sample characterizations via x-ray measurements

Specular x-ray reflectivity was measured to characterize the layer thickness and the height of interfacial roughness of the sample. The beam source was a Cu x-ray tube with a 0.04 × 12-mm<sup>2</sup> line focus. The incident beam was defined by a 0.05-mm-wide slit prior to the sample. The angular resolution of the primary beam was measured to be 0.025° full width at half maximum (FWHM). A graphite analyzer was mounted after the sample to monochromatize the beam to the Cu K<sub>α</sub> wavelength, λ = 1.54 Å. Figure 1 shows the specular x-ray reflectivity

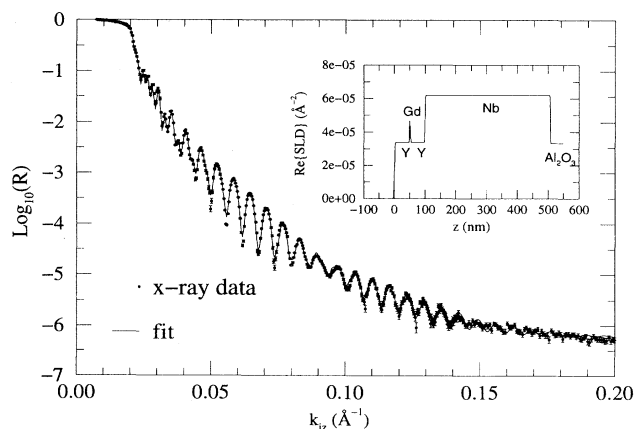


FIG. 1. X-ray specular reflectivity from the Y/Gd/Y/Nb/Al<sub>2</sub>O<sub>3</sub> sample. The laterally averaged depth profile of the sample, such as the thickness of various layers and the height of interfacial roughness, can be obtained from model fitting (solid line) to the data (filled circles). The inset shows the real part of the x-ray scattering length density (SLD) profile as a result of the fitting.

data (circles) and a least-squares fit (solid line) to the data. The  $k_{iz}$  is the  $z$  component of the incident wave vector where the  $z$  axis is defined normal to the sample surface, zero at the surface, and positive into the sample. As a result of the fitting, the layer thickness and interfacial roughness parameters were determined with less than 0.5 nm uncertainty. The inset of Fig. 1 shows the real part of the x-ray SLD as a function of  $z$ . The first Y layer thickness is 49.4 nm, in which the top 4 nm has a SLD lower than that of the bulk Y, indicating possible surface oxidation or water molecule adsorption besides surface roughness. The Gd layer is 3.2 nm thick, with interfacial roughness  $\sigma = 1.3$  nm (Y/Gd) and 3.0 nm (Gd/Y), where  $\sigma$  denotes the laterally averaged height of a Gaussian random roughness in FWHM. For the second Y layer, the thickness is 48.0 nm and the roughness is  $\sigma = 2.8$  nm (Y/Nb). The Nb layer is 407 nm thick and the roughness is  $\sigma = 1.8$  nm (Nb/Al<sub>2</sub>O<sub>3</sub>).

X-ray diffraction measurements were taken with a four-circle x-ray diffractometer to verify the crystal structure of each layer. Nearly parallel to the sample surface three crystal lattice planes were found parallel to each other: Al<sub>2</sub>O<sub>3</sub>(11 $\bar{2}$ 0)  $\parallel$  Nb(110)  $\parallel$  Y/Gd/Y(0001). In plane, the lattice orientations were found to be Al<sub>2</sub>O<sub>3</sub>[0001]  $\parallel$  Nb[1 $\bar{1}$ 1] and Nb[1 $\bar{1}$ 0]  $\parallel$  Y/Gd/Y[01 $\bar{1}$ 0]. The lattice constants evaluated from the data were consistent with the bulk values within the relatively coarse beam resolution.

Further x-ray-diffraction experiments were carried out to measure the miscut angle of the sample surface with respect to the Al<sub>2</sub>O<sub>3</sub>(11 $\bar{2}$ 0), Nb(110), and Y/Gd/Y(0001) planes, as well as the mosaic spread of these planes, using the x-ray reflectometer described earlier. With the tight resolution of the incident beam we could align the sample surface parallel to the incident beam within a  $\pm 0.01^\circ$  uncertainty. The sample rotation angle was initialized to zero at this position. In the subsequent measurements of the Al<sub>2</sub>O<sub>3</sub>(11 $\bar{2}$ 0), Nb(110), and Y/Gd/Y(0001) Bragg peaks, the difference between the sample rotation angle and half of the detector rotation angle was recorded. This extra amount of sample rotation needed to bring the lattice plane into Bragg reflection is the surface miscut angle in the particular in-plane direction parallel to the incident x-ray beam. We then rotated the sample about its surface normal and repeated the measurement to obtain the miscut angle along several different in-plane directions. The observed miscut angles  $\Delta\varphi_j$  are related to a maximum miscut angle  $\Delta\varphi_m$  by a cosine function,  $\Delta\varphi_j = \Delta\varphi_m \cos(\phi_j - \phi_0)$ , where  $j$  enumerates the in-plane directions, and  $\phi_j$  is the angle between this in-plane direction and an arbitrary in-plane reference line. Figure 2 shows the data of  $\Delta\varphi_j$  vs  $\phi_j$  for the Al<sub>2</sub>O<sub>3</sub>(11 $\bar{2}$ 0), Nb(110), and Y/Gd/Y(0001) peaks, respectively. Lines in Fig. 2 are fits of the cosine function to each set of data. The fitted values of  $\Delta\varphi_m$  are  $0.47^\circ \pm 0.01^\circ$  for Al<sub>2</sub>O<sub>3</sub>,  $0.46^\circ \pm 0.01^\circ$  for Nb, and  $0.43^\circ \pm 0.01^\circ$  for Y/Gd/Y, respectively. As observed from these values, the miscut of the substrate was essentially replicated layer by layer in the epitaxial growth. The in-plane direction for the maximum miscut, corresponding to  $\phi = \phi_0$ , was found to be  $2.2^\circ \pm 0.5^\circ$  from the Nb[001] direction. The sample rocking curve widths for the Al<sub>2</sub>O<sub>3</sub>(11 $\bar{2}$ 0), Nb(110),

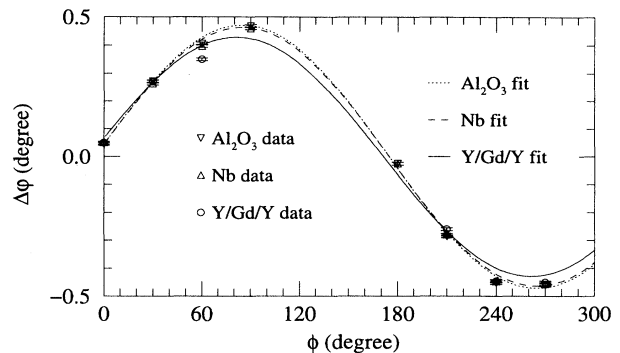


FIG. 2. X-ray measurements of the surface miscut angle as a function of in-plane direction. The solid lines are fits to the data with a model of  $\Delta\varphi = \Delta\varphi_m \cos(\phi - \phi_0)$  where  $\Delta\varphi_m$  is the maximum miscut angle between the sample surface and the intended lattice plane. The fitted values of  $\Delta\varphi_m$  are  $0.47^\circ \pm 0.01^\circ$  for Al<sub>2</sub>O<sub>3</sub>(11 $\bar{2}$ 0),  $0.46^\circ \pm 0.01^\circ$  for Nb(110), and  $0.43^\circ \pm 0.01^\circ$  for Y/Gd/Y(0001), respectively.

and Y/Gd/Y(0001) Bragg peaks were also measured at each sample orientation (enumerated by  $j$ ) in order to evaluate the mosaic spread of these lattice planes, which may be considered as a continuous distribution of the surface miscut angle. The rocking curve widths for the Al<sub>2</sub>O<sub>3</sub>(11 $\bar{2}$ 0) and Nb(110) planes were measured to be  $0.09^\circ$  which was resolution limited, while those for the Y/Gd/Y(0001) plane were  $0.29^\circ \pm 0.02^\circ$ . After deconvolved with the instrumental resolution, the mosaic spread of the Y/Gd/Y(0001) plane was determined to be  $0.28^\circ \pm 0.02^\circ$  in FWHM.

### C. Neutron experiments

We chose to investigate the grazing-incidence neutron diffraction from the Y/Gd/Y(1 $\bar{1}$ 00) plane. If there had been no surface miscut, the reciprocal vector  $\mathbf{Q}(1\bar{1}00)$  would have been exactly parallel to the sample surface. In the real sample, however,  $\mathbf{Q}(1\bar{1}00)$  was exactly perpendicular to the Y/Gd/Y[0001] axis while the Y/Gd/Y[0001] axis was deviated from the surface normal ( $z$  axis) by  $\Delta\varphi_m$ , which was measured with x rays to be normally distributed at  $0.43^\circ \pm 0.01^\circ$  with a FWHM of  $0.28^\circ \pm 0.02^\circ$ . Due to the  $60^\circ$  rotational symmetry about the Y/Gd/Y[0001] hexagonal axis, there were six  $\mathbf{Q}$ 's equivalent to  $\mathbf{Q}(1\bar{1}00)$ . In contrast, the Nb and Al<sub>2</sub>O<sub>3</sub> lattices only possessed twofold in-plane rotational symmetry. In addition, calculation showed that no reciprocal lattice vectors of the Nb and Al<sub>2</sub>O<sub>3</sub> lattices were in the vicinity of any one of the six  $\mathbf{Q}$ 's of Y/Gd/Y. This natural elimination of diffraction background from the buffer and substrate came from the special epitaxy of the Y/Gd/Y/Nb/Al<sub>2</sub>O<sub>3</sub> sample, and it would help us to clearly demonstrate diffraction of standing waves by the Y/Gd/Y film alone. In general, however, discrimination against the diffraction background in the grazing-incidence geometry will be achieved by the spa-

tial nonuniformity of the neutron waves and resonance enhancement.

The neutron experiments were carried out at the NG-7 reflectometer at the National Institute of Standards and Technology Cold Neutron Research Facility. The monochromated neutrons had an average wavelength of  $\lambda = 4.1 \text{ \AA}$  with  $\Delta\lambda/\lambda = 0.025$ . The distance from the monochromator to the sample was 200 cm. The incident beam was defined by two horizontal slits,  $S_1$  and  $S_2$ , located 160 cm and 20 cm prior to the sample, respectively. The sample was mounted face up horizontally on a goniometer which had three orthogonal rotational axes to adjust the sample orientation. The specular reflectivity was measured with a single detector. Two horizontal slits,  $S_3$  and  $S_4$ , located 20 cm and 200 cm after the sample, were used to collimate the reflected beam. To measure the diffraction intensity, a linear position-sensitive detector (PSD), 5 cm wide and 10 cm high, was placed 71 cm away from the sample. The channel height of the multichannel PSD was measured to be  $0.4591 \pm 0.0003 \text{ mm/channel}$ , and the resolution was measured to be four channels in FWHM. The vertical resolution for the diffracted beam was then  $0.15^\circ$  in FWHM. No slits were used to collimate the diffracted beam. Figure 3 is a schematic of the neutron beam configuration.

The sample was aligned at  $k_{iz} = 0.007 \text{ \AA}^{-1}$ . The Bragg angle at the given neutron wavelength was  $40.4^\circ$ , so the PSD was positioned about  $99.2^\circ$  away from the primary beam direction. Once the sample was aligned for the reflectivity measurement, diffraction intensity was optimized by rotating the sample about the  $z$  axis and adjusting the PSD position.

Once the sample was aligned, the specular reflection intensity and diffraction intensity were measured simultaneously. The sample alignment and data collection were repeated as the sample was rotated about the  $z$  axis at  $60^\circ$  increments. The integrated intensity on the PSD remained the same at all six different sample orientations, while the intensity distribution on the PSD varied sig-

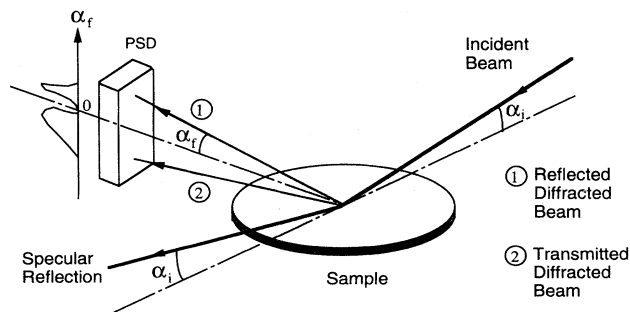


FIG. 3. A schematic of the neutron beam configuration for the diffraction experiments in grazing-incidence geometry. A linear position-sensitive detector (PSD) with 256 channels is used to record the diffraction intensity distribution as a function of the exit angle  $\alpha_f$ . The diffraction beam at  $\alpha > 0$  is named reflected diffracted beam and that at  $\alpha < 0$  transmitted diffracted beam.

nificantly and repeatably. From these observations one could draw preliminary conclusions that the diffraction signals seemed to come only from the Y/Gd/Y film, not from the Nb buffer or  $\text{Al}_2\text{O}_3$  substrate, and the sixfold in-plane rotational symmetry of the Y/Gd/Y film was broken, most likely by the seemingly small surface miscut.

We then selected two opposite in-plane orientations among the six for detailed measurements. The corresponding reciprocal lattice vector  $\mathbf{Q}$  was  $58^\circ$  and  $122^\circ$ , respectively, from the in-plane direction for the maximum miscut we defined earlier by  $\phi = \phi_0$  in  $\Delta\varphi = \Delta\varphi_m \cos(\phi - \phi_0)$ . Later in the data analysis we will show that it is the effective miscut angle in the  $\mathbf{Q}$  direction that enters the quantitative calculation. The effective miscut angle was then centered at  $\Delta\varphi = +0.23^\circ$  for  $\phi = 58^\circ$  (let  $\phi_0 = 0$ ) and  $\Delta\varphi = -0.23^\circ$  for  $\phi = 122^\circ$ . The FWHM of the  $\Delta\varphi$  distribution was still  $0.28^\circ \pm 0.02^\circ$ .

At each of the two sample orientations, neutron specular reflection and diffraction intensities were measured as a function of  $k_{iz}$ , which was increased from  $0.004 \text{ \AA}^{-1}$  to  $0.0125 \text{ \AA}^{-1}$  at a  $0.00025 \text{ \AA}^{-1}$  step. The vertical widths of the beam-defining slits  $S_1$  and  $S_2$  were incremented accordingly to keep the illuminated sample area a constant. The resultant incident beam resolution in the vertical direction was  $\Delta k_{iz}/k_{iz} \simeq 0.053$ . Because of low diffraction intensity, we counted for 1 h at each  $k_{iz}$ . The maximum diffraction intensity registered on the PSD was  $\sim 120$  neutron/channel/h. The radiation background was about seven neutron/channel/h at  $k_{iz} = 0.004 \text{ \AA}^{-1}$  and 14 neutron/channel/h at  $k_{iz} = 0.012 \text{ \AA}^{-1}$ . The larger radiation background was due to the increase in the slit widths of  $S_1$  and  $S_2$ .

The reflectivities for  $\phi = 58^\circ$  and  $\phi = 122^\circ$  were similar. Figure 4 shows the result for  $\phi = 122^\circ$ . The ex-

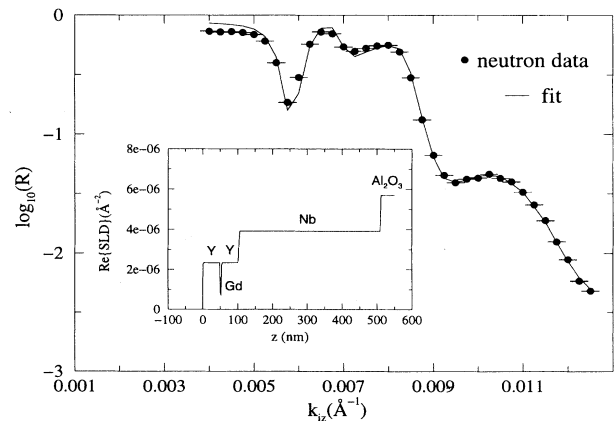


FIG. 4. Neutron specular reflectivity from the Y/Gd/Y/Nb/ $\text{Al}_2\text{O}_3$  sample at  $\phi = 122^\circ$ . The solid line is a fit to the data. The dips below  $k_{iz} = 0.0085 \text{ \AA}^{-1}$  (the critical  $k_{iz}$  of  $\text{Al}_2\text{O}_3$  for total external reflection) are due to neutron absorption by Gd nuclei, not the in-plane diffraction process. The specular reflectivity remains essentially the same at  $\phi = 58^\circ$ , and other values where in-plane diffraction conditions are not met. The inset is the real part of the neutron SLD profile as a result of the model fitting.

perimental data are shown with circles. The dips in the neutron reflectivity below the critical  $k_{iz}$  of  $\text{Al}_2\text{O}_3$  for total reflection ( $0.0085 \text{ \AA}^{-1}$ ) were due to the resonance-enhanced neutron absorption by the Gd layer,<sup>28</sup> not diffraction, which was too weak to perturb the reflectivity substantially. The solid line in Fig. 4 is a least-squares fit to the data. The composition depth profile obtained from the fitting is consistent with the x-ray result.

Figure 5 shows the diffraction intensity distribution on the PSD taken at  $k_{iz} = 0.006 \text{ \AA}^{-1}$  for (a)  $\phi = 122^\circ$  and (b)  $\phi = 58^\circ$ . The data are shown with circles. The channel number has been converted to the final exit angle  $\alpha_f$  which is defined to be positive above the sample horizon and negative below. The  $\alpha_f = 0^\circ$  position on the PSD was experimentally determined with a  $0.1^\circ$  uncertainty. The diffraction intensity, after a background subtraction, has been normalized to the incident beam intensity intercepted by the sample. The solid line is from model calculation, which will be explained in the data analysis section.

One way to display the dependence of the diffraction intensity as a function of  $k_{iz}$  is to integrate the intensity over  $\alpha_f$  and plot the  $\alpha_f$ -integrated intensity as a function of  $k_{iz}$ . Figure 6 shows the  $\alpha_f$ -integrated intensity over  $\alpha_f > 0$  as a function of  $k_{iz}$  for  $\phi = 122^\circ$  (filled circle) and  $\phi = 58^\circ$  (open square). The solid lines are results of model calculations which will be explained in the data analysis section. There we will show that the peaks in

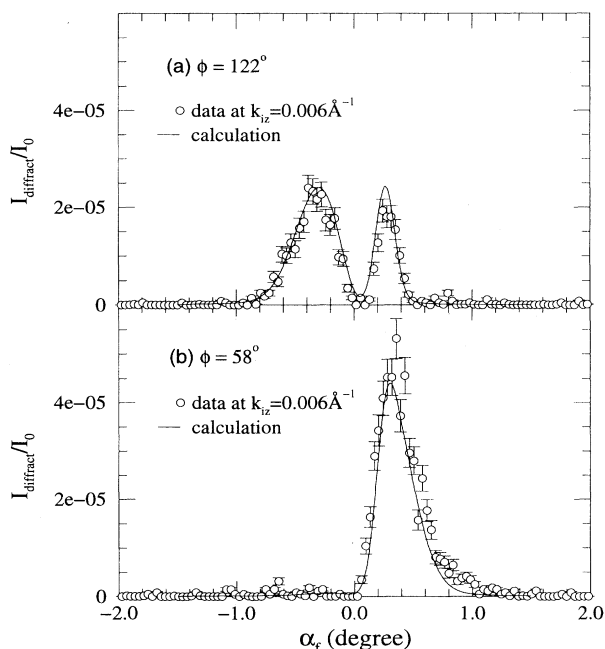


FIG. 5. The neutron diffraction intensity at  $k_{iz} = 0.006 \text{ \AA}^{-1}$  as a function of  $\alpha_f$  for (a)  $\phi = 122^\circ$  and (b)  $\phi = 58^\circ$ , respectively. The background-subtracted intensity has been normalized to the incident beam intensity intercepted by the sample surface. Solid lines are results of theoretical calculations. The difference between the diffraction patterns of (a) and (b) is due to the surface miscut.

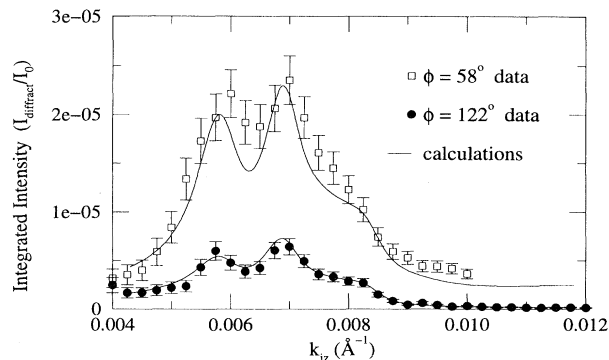


FIG. 6. The neutron diffraction intensity integrated over  $\alpha_f > 0$  as a function of  $k_{iz}$  for  $\phi = 58^\circ$  and  $122^\circ$ . Solid lines are results of theoretical calculations. Peaks near  $k_{iz} = 0.006 \text{ \AA}^{-1}$  and  $0.007 \text{ \AA}^{-1}$  are due to resonance enhancement of the neutron standing waves in the Y/Gd/Y film.

the diffraction intensity near  $k_{iz} = 0.006 \text{ \AA}^{-1}$  and  $0.007 \text{ \AA}^{-1}$  are due to resonance enhancement of the neutron standing waves in the Y/Gd/Y film.

### III. DATA ANALYSIS

In this section we will first briefly describe the general scheme of how to calculate the neutron-scattering cross section of grazing-incidence diffraction by a mosaic thin film; more details can be found elsewhere.<sup>25</sup> Then the result will be applied to analyze the data of the present experiment.

#### A. The kinematic theory

For a mosaic thin film, the neutron diffraction in the grazing-incidence geometry is generally weak, and the scattering cross section can be calculated in the kinematic limit by using the distorted-wave Born approximation (DWBA). In brief, the neutron waves of the first-order approximation in DWBA are not plane waves in free space as used in the Born approximation, but rather the spatially nonuniform waves in the sample which are “distorted” by reflection and refraction. A general description of DWBA in quantum-mechanical scattering theory can be found in standard text books,<sup>32</sup> and applications to neutron and x-ray surface scattering can be found in the literature.<sup>4-6,12,13,24,25,33,34</sup> Results pertaining to the present case of grazing-incidence diffraction of neutron standing waves by thin films can be concisely given as follows.

The differential cross section can be generally written as

$$\frac{d\sigma}{d\Omega} = \left| \iiint \psi_f^*(\mathbf{r}, \mathbf{k}_f) V(\mathbf{r}) \psi_i(\mathbf{r}, \mathbf{k}_i) d^3\mathbf{r} \right|^2, \quad (3.1)$$

where

$$V(\mathbf{r}) = \sum b_j \delta(\mathbf{r} - \mathbf{r}_j) \quad (3.2)$$

is the scattering potential in which  $j$  enumerates all scattering nuclei,  $b_j$  is the coherent scattering length of the  $j$ th nucleus, and  $\mathbf{r}_j$  is its position. The initial wave function  $\psi_i(\mathbf{r}, \mathbf{k}_i)$  is the solution of the Schrödinger equation

$$\hat{H}\psi = E\psi, \quad (3.3)$$

with a Hamiltonian,

$$\hat{H} = \hat{H}_0 + V_1(z), \quad (3.4)$$

where  $V_1(z)$  is the lateral average of  $V(\mathbf{r})$ , and the initial condition is assumed to be  $\psi_i(\mathbf{r}, \mathbf{k}_i) \sim e^{i\mathbf{k}_i \cdot \mathbf{r}}$ . The final wave function  $\psi_f(\mathbf{r}, \mathbf{k}_f)$  is the time-reversed solution of Eq. (3.3) and Eq. (3.4), with an initial condition  $\psi_f(\mathbf{r}, \mathbf{k}_f) \sim e^{i(-\mathbf{k}_f) \cdot \mathbf{r}}$ . The “distortion” effect of reflection and refraction is taken into account by including  $V_1(z)$  in the first-order approximation to the full Hamiltonian  $\hat{H} = \hat{H}_0 + V(r)$ .

The differential cross section can be written more ex-

PLICITLY given the translational symmetry of the wave functions  $\psi_i(\mathbf{r}, \mathbf{k}_i)$  and  $\psi_f(\mathbf{r}, \mathbf{k}_f)$  in the  $x$ - $y$  plane, and a small surface miscut angle  $\Delta\varphi_m$ . In such circumstances the wave functions can be written as

$$\psi_i(\mathbf{r}, \mathbf{k}_i) = e^{i(k_{ix}x + k_{iy}y)} \psi_i(z, k_{iz}), \quad (3.5)$$

$$\psi_f(\mathbf{r}, \mathbf{k}_f) = e^{i(k_{fx}x + k_{fy}y)} \psi_f(z, k_{fz}), \quad (3.6)$$

and the  $\mathbf{r}_j$  in Eq. (3.2) can be expressed as, for instance of an orthogonal lattice,

$$\mathbf{r}_j = n_1 a_1 \hat{\mathbf{x}}' + n_2 a_2 \hat{\mathbf{y}}' + n_3 a_3 \hat{\mathbf{z}}' + \hat{\mathbf{r}}', \quad (3.7)$$

where  $\hat{\mathbf{x}}'$ ,  $\hat{\mathbf{y}}'$ , and  $\hat{\mathbf{z}}'$  are unit vectors of a new Cartesian coordinate system which is rotated from  $\hat{\mathbf{x}}$ ,  $\hat{\mathbf{y}}$ , and  $\hat{\mathbf{z}}$  by  $\Delta\varphi_m$ ,  $0 \leq n_1 \leq N_1 - 1$ ,  $0 \leq n_2 \leq N_2 - 1$ , and  $0 \leq n_3 \leq N_3 - 1$ , and  $\hat{\mathbf{r}}'$  is the relative position of the  $j$ th nucleus in the unit cell  $(n_1, n_2, n_3)$ . Assuming that there are  $m - 1$  layers in a thin-film sample on a substrate labeled  $m$ , we denote the interfacial positions by  $z_1 = 0$ ,  $z_2 = d_1, \dots$ , and  $z_m = z_{m-1} + d_{m-1}$ . Let  $\mathbf{Q} = (k_{fx} - k_{ix})\hat{\mathbf{x}} + (k_{fy} - k_{iy})\hat{\mathbf{y}}$ , the differential cross section can be written as

$$\begin{aligned} \frac{d\sigma}{d\Omega} \approx & \left| \sum_{l=1}^m F_l(\mathbf{Q}) \frac{1 - e^{-iN_{1l}\mathbf{Q} \cdot \mathbf{a}_{1l}}}{1 - e^{-i\mathbf{Q} \cdot \mathbf{a}_{1l}}} \frac{1 - e^{-iN_{2l}\mathbf{Q} \cdot \mathbf{a}_{12}}}{1 - e^{-i\mathbf{Q} \cdot \mathbf{a}_{12}}} \right. \\ & \times \left. \sum_{n_{13}=0}^{N_{13}-1} \psi_f^*(z_1 + n_{13}a_{13}, k_{fz}) \psi_i(z_1 + n_{13}a_{13}, k_{iz}) e^{-i|\mathbf{Q}|\Delta\varphi(z_1 + n_{13}a_{13})} \right|^2 \end{aligned} \quad (3.8)$$

where  $F_l(\mathbf{Q})$  is the structure factor and  $\Delta\varphi$  is the effective surface miscut angle in the  $\mathbf{Q}$  direction. It should be noted that in Eq. (3.8) we have assumed that the scattering from all  $m$  layers is added coherently. In the opposite case where scattering from each layer is added incoherently, one should add the intensities first (the absolute value squared) and then sum over  $l$  from 1 to  $m$ .

We note that these equations apply to the evanescent scattering as well, which can be seen as a special case with a bare substrate without the film. The diffraction of standing waves and resonance enhancement, however, occur only when the film is present, via the wave functions  $\psi_i(z, k_{iz})$  and  $\psi_f(z, k_{fz})$  above a total reflection surface.

As a general approach to simulate the experimental data, functions in the first-order approximation, such as  $V_1(z)$  and  $\psi_i(z, k_{iz})$ , can be generated by fitting a model calculation to neutron and x-ray specular reflectivity data, as routinely done in neutron and x-ray reflectometry. In calculating  $\psi_f(z, k_{fz})$  from the generated  $V_1(z)$ , however, it should be noted that different solutions arise depending on whether  $k_{fz} > 0$  or  $k_{fz} < 0$ . If  $k_{fz} > 0$ , the initial wave function with  $-k_{fz}$  comes from the vacuum side, and the solution is similar to  $\psi_i(z, k_{iz})$  with

only  $k_{iz}$  replaced by  $-k_{fz}$ . In this case, the diffracted beam comes out of the sample surface back to the vacuum, and is therefore called the reflected diffracted beam (RDB). If  $k_{fz} < 0$ , on the other hand, the initial wave function with  $-k_{fz}$  comes from the substrate side, and the scattering potential is that of the  $m$  layers in reversed stacking, which then gives a completely different wave function. In this case, the diffracted beam goes into the substrate, and eventually merges out from one side of the substrate. This part of the diffracted beam may be called the transmitted diffracted beam (TDB). With x rays, due to high absorption of the substrate, the TDB may not be observable, but with neutrons it is easily seen, as evidenced in the present experiment, as well as in earlier experiments of evanescent neutron scattering.<sup>15-19</sup> We note that the intensity of the TDB has not been quantitatively calculated before,<sup>15-19</sup> and the direction of the TDB has been predicted<sup>16-19</sup> for the zero-miscut case to be  $\alpha_f = 0$  which, in our opinion, is incorrect. The theory given above always gives a zero intensity in the  $\alpha_f = 0$  direction for both standing-wave diffraction and evanescent-wave diffraction.

Once the functions in the first-order approximation are known, one is ready to model the 2D lattice struc-

tures and use equations such as Eq. (3.8) to calculate the diffraction cross section, which is proportional to the diffraction intensity. To compare with the experimental data, one needs to further take into account finite instrumental resolutions of both incident beam and exit beam, as well as the distribution of the surface miscut angle  $\Delta\varphi$  due to the mosaic spread of the lattice planes.

### B. Application to Y/Gd/Y/Nb/Al<sub>2</sub>O<sub>3</sub>

We used Eq. (3.8) to calculate the diffraction intensity for the  $\mathbf{Q}(1\bar{1}00)$  peak of the Y/Gd/Y lattice. Because of the loose horizontal collimation of the primary beam, the diffraction intensity should be integrated over  $Q_x$  and  $Q_y$ . We then only need to calculate

$$\left| \sum_{l=1}^3 F_l(\mathbf{Q}) \sum_{n_{13}=0}^{N_{13}-1} \psi_f^*(z_l + n_{13}a_{13}, k_{fz}) \psi_i(z_l + n_{13}a_{13}, k_{iz}) \times e^{-i|\mathbf{Q}|\Delta\varphi(z_l + n_{13}a_{13})} \right|^2 \quad (3.9)$$

as a function of  $(k_{iz}, k_{fz})$ , which should scale to the diffraction intensity by a single constant. The wave functions  $\psi_i$  and  $\psi_f^*$  were easily generated given the potential  $V_1(z)$  which was determined from the neutron and x-ray reflectivity data. The lattice parameters and the effective surface miscut angles were predetermined using the x-ray-diffraction data. As for  $N_{13}$ , we tentatively assumed sharp boundaries at the interfaces, as the effect of the interdiffusion on the diffraction intensity was expected to be a second-order correction for this sample. The instrumental resolution parameters were also experimentally predetermined. We would like to emphasize that for the calculational results shown in Fig. 5 and Fig. 6, there is only one adjustable parameter, which is the intensity-scale constant independent of  $k_{iz}$ ,  $k_{fz}$ , and  $\Delta\varphi$ .

The solid line in Fig. 5 shows the calculated intensity at  $k_{iz} = 0.006 \text{ \AA}^{-1}$  as a function of  $\alpha_f$  for (a)  $\phi = 122^\circ$  and (b)  $\phi = 58^\circ$ , respectively. Since we know that the effective surface miscut angle  $\Delta\varphi$  has a Gaussian distribution centered at  $\pm 0.23^\circ$  with  $0.28^\circ$  FWHM, the calculated intensity has been first convoluted with this Gaussian distribution. The intensity has been further convoluted with the PSD resolution of  $0.15^\circ$  FWHM in  $\alpha_f$ . As for the incident beam, the angular divergence at  $k_{iz} = 0.006 \text{ \AA}^{-1}$  is only  $0.01^\circ$  FWHM and convolution is not necessary. The excellent agreement between the data and the calculation confirms that the difference between the diffraction patterns for  $\phi = 122^\circ$  and  $\phi = 58^\circ$  indeed arises from the surface miscut.

The solid lines in Fig. 6 show the calculated intensities integrated over  $\alpha_f > 0$  as functions of  $k_{iz}$  for  $\phi = 122^\circ$  and  $\phi = 58^\circ$ . The intrinsic intensity has been convoluted with the incident beam resolution,  $\Delta k_{iz} \simeq 0.053 k_{iz}$ . Peaks near  $k_{iz} = 0.006 \text{ \AA}^{-1}$  and  $0.007 \text{ \AA}^{-1}$  are due to resonance enhancement of the neutron standing waves

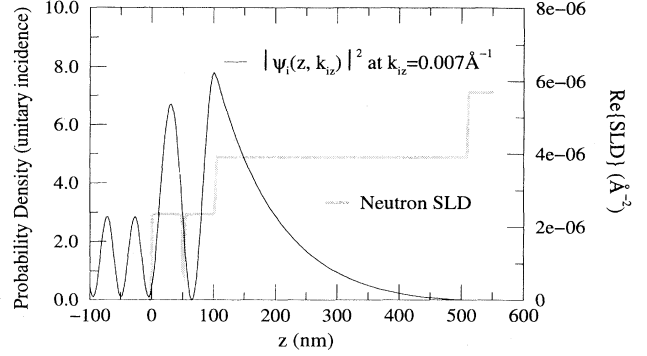


FIG. 7. Probability density  $|\psi_i(z, k_{iz})|^2$  at  $k_{iz} = 0.007 \text{ \AA}^{-1}$  (thin solid line) together with the real part of the neutron SLD profile (thick grey line). Standing waves in the  $z$  direction are created above the Nb buffer at  $k_{iz} \leq 0.007 \text{ \AA}^{-1}$ , and they are resonantly amplified in the Y/Gd/Y film at  $k_{iz} = 0.007 \text{ \AA}^{-1}$  (and  $0.006 \text{ \AA}^{-1}$  for the first resonance mode). The  $|\psi_i(z, k_{iz})|^2$  is the flux of the “distorted” neutron wave traveling in the  $x$ - $y$  plane, and its peak value becomes about 7 times greater than the unitary flux of the original incident plane wave.

being diffracted, where the Nb buffer serves as the total-reflection mirror. Many more resonance peaks are found in the intrinsic intensity above  $k_{iz} = 0.007 \text{ \AA}^{-1}$ , where the Al<sub>2</sub>O<sub>3</sub> substrate serves as the total-reflection mirror; however, they are smeared by the coarser  $k_{iz}$  resolution at the higher  $k_{iz}$  range.

One can plot the “distorted” wave function in the sample at a certain resonance mode to find out the enhancement factor. Figure 7 shows the  $|\psi_i(z, k_{iz})|^2$  at  $k_{iz} = 0.007 \text{ \AA}^{-1}$ , together with the real part of the neutron SLD profile for comparison. The maximum neutron flux is about 7 times greater than the unitary flux of the original incident plane wave. It should be noted that the enhancement factor could be much larger if the strong absorption by the Gd nuclei were not present.

## IV. CONCLUSIONS

In the same spirit of using spatially nonuniform neutron and x-ray waves as in the evanescent scattering to achieve concentrated diffraction from the surface of a bulk crystal, we have used neutron and x-ray standing waves in thin films for diffraction experiments, which in principle can discriminate against possible diffraction background from the buffer or substrate, especially when the standing waves are resonantly amplified, and can provide variable spatial modulation within the film. We have experimentally demonstrated the diffraction of neutron standing waves and resonance enhancement via a Y/Gd/Y/Nb/Al<sub>2</sub>O<sub>3</sub> sample, and applied a quantitative calculation which describes the diffraction pattern in the grazing-incidence geometry very well. We anticipate that further improved sample engineering will increase the resonance-enhancement factor by manifold, and further skillful applications of the diffraction geometry will shed light on the study of 2D magnetic and crystal structures and phase transitions in thin films.

- <sup>1</sup> W. C. Marra, P. Eisenberger, and A. Y. Cho, *J. Appl. Phys.* **50**, 6927 (1979).
- <sup>2</sup> P. Eisenberger and W. C. Marra, *Phys. Rev. Lett.* **46**, 1081 (1981).
- <sup>3</sup> W. C. Marra, P. H. Fuoss, and P. Eisenberger, *Phys. Rev. Lett.* **49**, 1169 (1982).
- <sup>4</sup> G. H. Vineyard, *Phys. Rev. B* **26**, 4146 (1982).
- <sup>5</sup> S. Dietrich and H. Wagner, *Phys. Rev. Lett.* **51**, 1469 (1983).
- <sup>6</sup> S. Dietrich and H. Wagner, *Z. Phys. B* **56**, 207 (1984); **59**, 35 (1985).
- <sup>7</sup> A. Zeilinger and T. J. Beatty, *Phys. Rev. B* **27**, 7239 (1983).
- <sup>8</sup> P. L. Cowan, *Phys. Rev. B* **32**, 5437 (1985).
- <sup>9</sup> P. L. Cowan, S. Brennan, T. Jach, M. J. Bedzyk, and G. Materlik, *Phys. Rev. Lett.* **57**, 2399 (1986).
- <sup>10</sup> T. Jach, P. L. Cowan, Q. Shen, and M. J. Bedzyk, *Phys. Rev. B* **39**, 5739 (1989).
- <sup>11</sup> T. Jach, D. B. Novotny, M. J. Bedzyk, and Q. Shen, *Phys. Rev. B* **40**, 5557 (1989).
- <sup>12</sup> H. Dosch, B. W. Batterman, and D. C. Wack, *Phys. Rev. Lett.* **56**, 1144 (1986).
- <sup>13</sup> H. Dosch, *Phys. Rev. B* **35**, 2137 (1987).
- <sup>14</sup> L. Mailänder, H. Dosch, J. Peisl, and R. L. Johnson, *Phys. Rev. Lett.* **64**, 2527 (1990).
- <sup>15</sup> K. Al Usta, H. Dosch, A. Lied, and J. Peisl, *Physica B* **173**, 65 (1991).
- <sup>16</sup> H. Dosch, K. Al Usta, A. Lied, W. Drexel, and J. Peisl, *Rev. Sci. Instrum.* **63**, 5533 (1992).
- <sup>17</sup> H. Dosch, *Physica B* **192**, 163 (1993).
- <sup>18</sup> H. Dosch, *Neutron News* **6**, 19 (1995).
- <sup>19</sup> H. Dosch, *Critical Phenomena at Surfaces and Interfaces, Evanescent X-Ray and Neutron Scattering* (Springer-Verlag, New York, 1992).
- <sup>20</sup> J. F. Ankner, H. Zabel, D. A. Neumann, C. F. Majkrzak, J. A. Dura, and C. P. Flynn, *J. Phys. (Paris) Colloq.* **50**, C7-189 (1989).
- <sup>21</sup> J. F. Ankner, C. F. Majkrzak, D. A. Neumann, A. Matheny, and C. P. Flynn, *Physica B* **173**, 89 (1991).
- <sup>22</sup> J. F. Ankner, in *Surface X-Ray and Neutron Scattering*, edited by H. Zabel and I. K. Robinson (Springer-Verlag, Berlin, 1992), p. 105.
- <sup>23</sup> J. Als-Nielsen, D. Jacquemain, K. Kjaer, F. Leveiller, M. Lahav, and L. Leiserowitz, *Phys. Rep.* **246**, 251 (1994).
- <sup>24</sup> S. Dietrich and A. Haase, *Phys. Rep.* **260**, 1 (1995).
- <sup>25</sup> Huai Zhang, *Physica B* (to be published).
- <sup>26</sup> J. Wang, M. J. Bedzyk, and M. Caffery, *Science* **258**, 775 (1992).
- <sup>27</sup> L. J. Norton, E. J. Kramer, R. A. L. Jones, F. S. Bates, H. R. Brown, G. P. Felcher, and R. Kleb, *J. Phys. (France) II* **4**, 1 (1994).
- <sup>28</sup> Huai Zhang, P. D. Gallagher, S. K. Satija, R. M. Lindstrom, R. L. Paul, T. P. Russel, P. Lambooy, and E. J. Kramer, *Phys. Rev. Lett.* **72**, 3044 (1994).
- <sup>29</sup> Y. P. Feng, S. K. Sinha, H. W. Deckman, J. B. Hastings, and D. P. Siddons, *Phys. Rev. Lett.* **71**, 537 (1993).
- <sup>30</sup> J. Kwo, E. M. Gyorgy, D. B. McWhan, M. Hong, F. J. Disalvo, C. Vettier, and J. E. Bower, *Phys. Rev. Lett.* **55**, 1402 (1985).
- <sup>31</sup> J. Kwo, D. B. McWhan, M. Hong, E. M. Gyorgy, L. C. Feldman, and J. E. Cunningham, in *Layered Structures, Epitaxy, and Interfaces*, edited by J. H. Gibson and L. R. Dawson, Material Research Society Symposia Proceedings No. 37 (Material Research Society, Pittsburgh, 1985), p. 509.
- <sup>32</sup> L. I. Schiff, *Quantum Mechanics* (McGraw-Hill, New York, 1955).
- <sup>33</sup> S. K. Sinha, E. B. Sirota, S. Garoff, and H. B. Stanley, *Phys. Rev. B* **38**, 2297 (1988).
- <sup>34</sup> J. P. Schlomka, M. Tolan, L. Schwalowsky, O. H. Seeck, J. Stettner, and W. Press, *Phys. Rev. B* **51**, 2311 (1995).